

3D Adaptive AUV Sampling for Classification of Water Masses

YaoLin Ge¹, Jo Eidsvik¹, and Tore Mo-Bjørkelund²

¹Department of Mathematical Sciences, Norwegian University of Science and
Technology, Trondheim, Norway

²Department of Marine Technology, Norwegian University of Science and
Technology, Trondheim, Norway

Abstract

Autonomous underwater vehicles with onboard computing units foster innovative approaches for sampling oceanographic phenomena. Feedback of observations via the onboard model to planning algorithms enable adaptive sampling for such robotic units. In this work we develop, implement and test an adaptive sampling algorithm for efficient sampling of water masses in a three-dimensional frontal system. Focusing on a river plume, salinity variations are used to characterize the water masses. A threshold in salinity is assumed to distinguish the ocean and river waters, so that excursions below the threshold define river waters. The onboard model builds on a Gaussian random field representation of the salinity variations in (north, east, depth) coordinates. This model is initially trained from numerical ocean model data, and then updated with data gathered by the agent. The Gaussian random field model further allows closed-form expressions of the expected spatially integrated Bernoulli variance of the salinity excursion set. Combining these results with forward-looking planning algorithms, we suggest a workflow for three-dimensional adaptive sampling to map river plume systems. Simulation studies are used to compare the suggested approach with others. Results of field trials in the Nidelva river plume in Norway are then presented and discussed.

Index Terms

AUV, adaptive sampling, path planning, excursion sets, river plume

yaolin.ge@ntnu.no

jo.eidsvik@ntnu.no

tore.mo-bjorkelund@ntnu.no

25

I. INTRODUCTION

26 A river plume is formed when the fresh water flowing out of the river encounters the saline
 27 water in the ocean [1]. When these two different water masses meet, they form a varying spatio-
 28 temporal boundary [2]. There have been increasing efforts using numerical models and data to
 29 investigate such phenomenon in the past decades [3, 4, 5, 6, 7, 8].

30 Autonomous underwater vehicles (AUVs) with onboard sensors and computing resources
 31 provide rich opportunities for oceanographic sampling as they can calibrate numerical ocean
 32 model outputs with in-situ data, and fill in the sampling resolution gaps at locations with large
 33 uncertainty [9, 10, 11, 12]. For frontal regions such as river plumes, AUV sampling is helpful
 34 for classifying the different water masses more accurately. Previous AUV sampling efforts focus
 35 mainly on pre-programmed sampling plans [13, 14]. Recent efforts have shown added value
 36 of having adaptive sampling plans [15, 16]. Adaptive sampling strategies here refer to AUV
 37 planning schemes that enable the AUV plan to be updated based on the posterior knowledge
 38 and the current situation. Ideas from statistical sampling design are highly useful in this field,
 39 because they can help guide the AUV to informative locations [15, 17].

40 The main contribution of this work is a three-dimensional (3D) full-scale adaptive AUV
 41 sampling strategy. With the AUVs limiting computing resources, a Gaussian random field (GRF)
 42 model serves as a statistical proxy models for the spatial salinity field in the 3D domain (north,
 43 east, depth). This 3D GRF model running onboard the AUV is sequentially refined, and this
 44 allows adaptive sampling. Starting with prior knowledge from a numerical ocean model, we
 45 use an AUV to adaptively explore the 3D boundary between the water masses in the river
 46 plume. We suggest algorithms to speed up design computations and to enable efficient robotic
 47 maneuverability [18]. We use a statistical design criterion based on the uncertainty of the
 48 Excursion Set (ES) of low salinity which distinguishes the river from the ocean water. This ES
 49 is defined by spatial locations having salinity level below a user-defined threshold. Building on
 50 recently developed closed form expressions [15] for the Expected Integrated Bernoulli Variance
 51 (EIBV) associated with the ES, we compare the EIBV associated with each candidate design
 52 location, and select the design which has the minimum EIBV. The EIBV is a useful criterion for
 53 improved classification of the river plume as it is large when probabilities of excursions are far
 54 from 0 or 1. One should select sampling designs that on expectation pull probabilities towards
 55 the 0 and 1 end-points to reduce the uncertainty of the ES.

56 Via simulation studies and *in-situ* measurements from the Nidelva river plume in Trondheim,
 57 Norway, we study the properties of the EIBV sampling plans in the 3D domain. For the real-
 58 world experiments we used a Light AUV (LAUV) [19] with an on-board NVIDIA Jetson TX2
 59 computing unit.

60 This paper is structured as follows. In Section II we provide the background and motivation for
 61 our work on adaptive AUV sampling to river plume water masses characterization. In Section
 62 III we introduce the models and methods used in this paper. In Section IV we present our
 63 implementation used for path planning. In Section V we show a simulation study illustrating
 64 the properties of our 3D adaptive sampling approaches. In Section VI we show results from
 65 the Nidelva river plume experiments. In Section VII we summarize our main contributions and
 66 findings and point to future work.

67 II. OCEAN SAMPLING

68 A. Data sources

69 Numerical solutions of the complex differential equations governing spatio-temporal oceanographic
 70 variation with boundary conditions and forcing are essential in understanding the ocean variability.
 71 In our application we rely on a fjord-scale implementation of the SINMOD software [20]. Such
 72 ocean model data provide physical interpretability of the ocean variability, but they often need
 73 calibration or bias adjustments, and there have been growing interests in uncertainty quantification
 74 and data assimilation methods for various scales of this challenge, see e.g. [21].

75 Traditional *in-situ* measurements generating input or calibration data to numerical ocean
 76 models include stationary or floating buoys, gliders, moorings and ships [22]. With the advent of
 77 smaller inexpensive sensor systems, one has capabilities of handling a variety of measurements
 78 for biological, chemical and oceanographic purposes [22]. Ships data can be expensive, and
 79 buoys and gliders have limited flexibility in maneuverability given coverage constraints [23].

80 Satellite imagery has been a powerful and useful tool for analyzing ocean variables. Data from
 81 satellites can provide a large-scale coverage of the entire field of interest, and even output portraits
 82 of river plumes [6]. However, due to large latency and uncertainty (cloud coverage issues) of
 83 obtaining such images, the usage of satellite imagery is limited. Satellite data unfavorably cover
 84 only the surface of the ocean [24].

85 The development of underwater robotics have led to a large number of robot-assisted applications
 86 in oceanography. Thanks to the flexibility of the robots, there are growing numbers of autonomous

87 sampling missions which are conducted by robots [9]. Benefits further include real-time sensing
 88 and high-resolution data gathering, with large opportunities to move in flexible paths in the ocean
 89 environment. In our case, an AUV is used as the target platform which is able to support 3D
 90 adaptive sampling at high resolution.

91 *B. Sequential AUV sampling*

92 We denote the salinity field by $\{\xi_{\mathbf{u}}; \mathbf{u} \in \mathcal{M} \subset \mathbb{R}^3\}$, where the location \mathbf{u} is (longitude,
 93 latitude, depth) and \mathcal{M} is the spatial domain. Initially, we specify a probabilistic model for the
 94 salinity based on numerical ocean model data. This provides a realistic initial model for the
 95 3D salinity characteristics, one that it is much more physically inspired than a simple linear
 96 regression from available in-situ AUV data [25]. We still use regression analysis to calibrate
 97 the 3D ocean model data to the real-world ocean experiment by using a short preliminary AUV
 98 survey [26]. The objective of the survey is not to reveal the entire field, but rather provide some
 99 *in-situ* measurements to adjust the ocean-model data and hence form a reasonable prior model
 100 for the day of deployment. Therefore, the path for the preliminary survey can be as simple as
 101 a transect line with yo-yo movements in the vertical direction. As mentioned in the previous
 102 section, one can also use satellite data or even drone images in this initial model specification,
 103 if such data are available [27].

104 *In-situ* salinity observations for the main part of the deployment are denoted by $\{\mathbf{y}_j; j =$
 105 $1, \dots, J\}$, for stages j of AUV measurements gathered over time. The vector \mathbf{y}_j of measurements
 106 at stage j , holds N_j measurements made according to spatial sampling design \mathbf{D}_j . The initial
 107 deployment location will then define \mathbf{D}_1 . We denote by $\mathcal{Y}_j = \{(\mathbf{y}_1, \mathbf{D}_1), \dots, (\mathbf{y}_j, \mathbf{D}_j)\}$ the
 108 collection of data gathered with the selected designs up to stage j . Initially, this is an empty set;
 109 $\mathcal{Y}_0 = \emptyset$.

110 The sequential designs are selected adaptively based on what is evaluated to be the most
 111 informative AUV sampling locations. In this evaluation, the on-board model is conditional to
 112 all the data gathered until the current time. With new observations available, data assimilation
 113 methods are used to update the probabilistic representation for the salinity variables. This means
 114 that the model is 'alive', and changing at every stage, depending on the data. Adaptive sampling
 115 fits into the diagram loop in Fig. 1. In our setting the spatial design plan is optimized based on the
 116 current spatial statistical model. Then the AUV gathers new observations according to the chosen
 117 design, and the spatial statistical model is updated. This continues over stages $j = 1, \dots, J$.

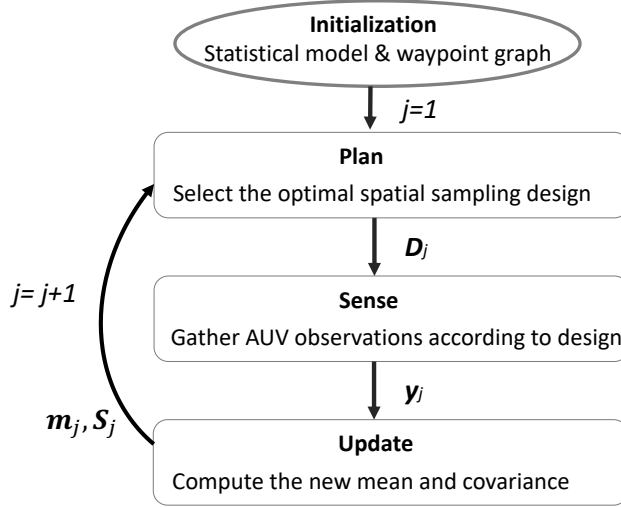


Fig. 1: Sequential loop where design D_j is chosen based on the updated model, y_j is the data collected in this design, and this is used to update the model (m_j, S_j) . This continues over stages $j = 1, 2, \dots, J$.

118 For prioritizing sampling efforts, one must impose an expected reward or value function
 119 associated with the different available sampling designs. At each stage, the expected rewards of
 120 all possible designs are evaluated. In our setting with river plumes, it makes sense to reward
 121 sampling locations that are expected to give data that improve the spatial characterization of the
 122 water masses [16, 15].

123 The setting is illustrated in Fig. 2, where we indicate the current location of the AUV, its path,
 124 and the sampling design opportunities at the current stage. The information criterion (EIBV) is
 125 calculated for all feasible designs, shown as circular dots. Here, smaller dots with lighter colors
 126 are indicative of larger expected uncertainty reduction. The adaptive sampling approach would
 127 act by moving to the location with lowest EIBV.

128 III. STATISTICAL MODELS AND METHODS FOR AUV SAMPLING

129 We next discuss our probabilistic modeling choices for the salinity field, and show how this
 130 enables efficient data assimilation as well as onboard design criteria. We then define ES and
 131 the EIBV as a design criterion, and finally present an adaptive sampling design algorithm for
 132 efficient 3D characterization of the river plume.

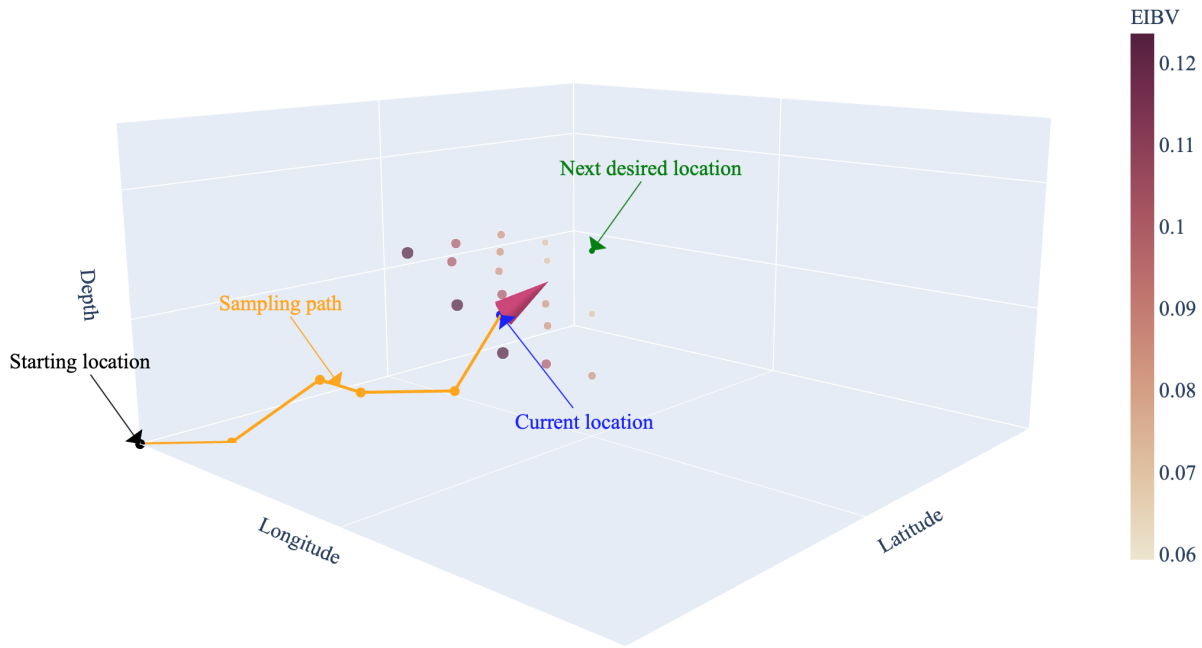


Fig. 2: An adaptive path example on a 3D waypoint graph. There are 16 candidate locations in different layers, the blue dot shows the current AUV location whereas the green dot indicates the desired next waypoint selected based on the minimum EIBV criterion.

¹³³ *A. On-board computing with GRFs*

¹³⁴ The prior model for river plume salinity $\{\xi_u, u \in \mathcal{M} \subset \mathbb{R}^3\}$, is defined via a GRF. A working
¹³⁵ assumption in our work is hence that the GRF provides a reasonable proxy model for the spatial
¹³⁶ salinity field in (latitude, longitude, depth). The initial model specification includes estimating the
¹³⁷ expected value of the field, its variability and spatial dependence. Note that the duration of the
¹³⁸ experiment will be short and the temporal variation in the river plume is ignored here. To check
¹³⁹ the Gaussian assumption, we made a quantile-quantile (QQ) plot from the SINMOD salinity
¹⁴⁰ data (Fig. 3). Here, we have computed the mean and variance at each location in a gridded
¹⁴¹ domain over replicates of time steps. The standardized residuals are used in the QQ plot. The
¹⁴² QQ plot in Fig. 3 shows a crossplot of the theoretical Gaussian quantile of the residuals against
¹⁴³ the empirical quantile of residuals in the data set. The blue line that we achieve is quite close
¹⁴⁴ to the straight line (red). Of course, the physical model does not give a Gaussian model, and
¹⁴⁵ we notice a sharper distribution near 0, but nevertheless the discrepancy is rather small.

Critically, the GRF model enables onboard data assimilation and adaptive AUV sampling

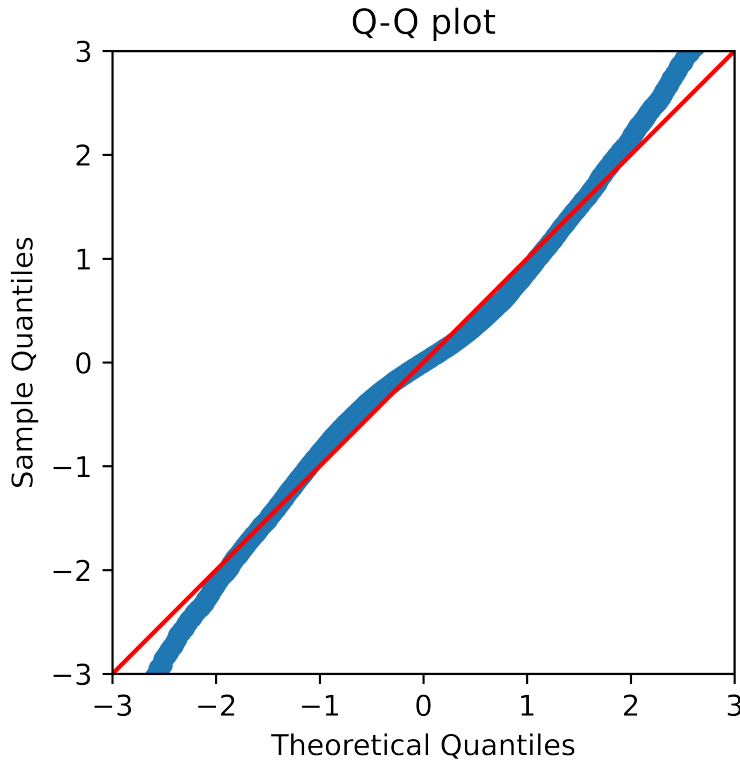


Fig. 3: Quantile-quantile plot of the residual based on SINMOD estimation. The residual is computed by subtracting the mean of the field and dividing the standard deviation.

efforts, as we will describe next. For onboard implementation and computing, the spatial domain is discretized to a set of n grid locations; $\{\mathbf{u}_1, \dots, \mathbf{u}_n\}$. This grid is also used for the waypoint graph setting for the AUV sampling design. The prior or initial GRF model at these grid locations is denoted by

$$\boldsymbol{\xi} = (\xi_{\mathbf{u}_1}, \dots, \xi_{\mathbf{u}_n})^T, \quad \boldsymbol{\xi} \sim N(\boldsymbol{\mu}, \boldsymbol{\Sigma}), \quad (1)$$

with associated probability density function (PDF) $p(\boldsymbol{\xi})$. Here, length- n vector $\boldsymbol{\mu}$ represents the prior mean of the 3D salinity variations, as will later be specified from ocean model data and a preliminary AUV transect run. The $n \times n$ covariance matrix $\boldsymbol{\Sigma}$ is defined via a Matérn covariance function with elements $\Sigma(i, i') = \sigma^2(1 + \phi_1 h(i, i')) \exp(-\phi_1 h(i, i'))$, where σ^2 is the variance and ϕ_1 a correlation decay parameter [28]. The distance between grid nodes \mathbf{u}_i and $\mathbf{u}_{i'}$ is defined for east, north and depth Euclidean distances via $h^2(i, i') = h_E^2(i, i') + h_N^2(i, i') + (\phi_1^2/\phi_2^2)h_D^2(i, i')$, with h being distance, and subscripts E, N, D indicating each of the three

153 directions in vector $\mathbf{u}_{i'} - \mathbf{u}_i$. Studies have shown that the lateral stretch of the river plume
 154 tends to be many magnitudes above the vertical stretch [1]. To model the correlation in different
 155 dimensions properly, we employ anisotropy between the lateral domain and the vertical domain.
 156 This means that the depth dimension is scaled differently (ϕ_2) using another correlation decay
 157 parameter than the one used in the lateral field (ϕ_1).

The measurements at each stage $j = 1, \dots, J$ are modeled by a Gaussian likelihood model

$$\mathbf{y}_j | \boldsymbol{\xi} \sim N(\mathbf{F}_j \boldsymbol{\xi}, \mathbf{R}_j), \quad (2)$$

158 where \mathbf{F}_j is an $N_j \times n$ selection matrix containing an entry of 1 in each row and 0 otherwise.
 159 The 1 entry refers to the sampling indices. With the covariance matrix $\mathbf{R}_j = r^2 \mathbf{I}_{N_j}$, we assume
 160 that the data are conditionally independent, given the underlying salinity. Here, r indicates the
 161 measurement standard deviation of the AUV salinity observations. We denote the associated PDF
 162 by $p(\mathbf{y}_j | \boldsymbol{\xi})$.

Via Bayes' rule, data assimilation at stages $j = 1, \dots, J$, gives the sequential conditional PDF
 $p(\boldsymbol{\xi} | \mathcal{Y}_j) \propto p(\mathbf{y}_j | \boldsymbol{\xi}) p(\boldsymbol{\xi} | \mathcal{Y}_{j-1})$. Under the assumptions about a GRF prior model and a Gaussian
 measurement error model, this conditional PDF is also Gaussian with mean \mathbf{m}_j and covariance
 matrix \mathbf{S}_j given by

$$\begin{aligned} \mathbf{G}_j &= \mathbf{S}_{j-1} \mathbf{F}_j^T (\mathbf{F}_j \mathbf{S}_{j-1} \mathbf{F}_j^T + \mathbf{R}_j)^{-1} \\ \mathbf{m}_j &= \mathbf{m}_{j-1} + \mathbf{G}_j (\mathbf{y}_j - \mathbf{F}_j \mathbf{m}_{j-1}) \\ \mathbf{S}_j &= \mathbf{S}_{j-1} - \mathbf{G}_j \mathbf{F}_j \mathbf{S}_{j-1}, \end{aligned} \quad (3)$$

163 where $\mathbf{m}_0 = \boldsymbol{\mu}$ and $\mathbf{S}_0 = \boldsymbol{\Sigma}$. The sequential updating resembles that of a spatio-temporal Kalman
 164 filter [28]. In our case, we study the benefits of using a 3D spatial model in the AUV sampling.
 165 Having a relatively short-term deployment, no explicit temporal dynamics are modeled.

166 *B. Excursion Set and Expected Integrated Bernoulli Variance*

We use the notion of an ES to characterize the river and ocean water masses [15]. The ES
 for salinity threshold t is defined by

$$\text{ES} = \{\mathbf{u} \in \mathcal{M} : \xi_{\mathbf{u}} \leq t\}. \quad (4)$$

Hence, salinity lower than this threshold will indicate river water. The associated excursion
 probability (EP) is

$$p_{\mathbf{u}} = P(\xi_{\mathbf{u}} \leq t), \quad \mathbf{u} \in \mathcal{M}. \quad (5)$$

When it is close to 1 or 0 at a given location, it is easy to classify the water mass to be river or ocean respectively. EP close to 0.5 reflects ambiguity in the characterization of water masses. The prior Bernoulli variance (BV) at location \mathbf{u} is $p_{\mathbf{u}}(1 - p_{\mathbf{u}})$ and the spatially integrated BV (IBV) is

$$\text{IBV} = \int p_{\mathbf{u}}(1 - p_{\mathbf{u}}) d\mathbf{u}, \quad (6)$$

¹⁶⁷ which is dominated by locations with probabilities near 0.5 and BV close 0.25. In practice the
¹⁶⁸ integral will be approximated by a sum over the n grid nodes.

¹⁶⁹ The goal is to construct AUV sampling strategies that prioritize locations that are ambiguous,
¹⁷⁰ thus making the exploration more effective. At each stage, we define the EIBV by

$$\begin{aligned} \text{EIBV}(\mathbf{D}_j) &= \int E_{\mathbf{y}_j | \mathcal{Y}_{j-1}; \mathbf{D}_j} [B_{\mathbf{u}}(\mathbf{y}_j)] d\mathbf{u}, \\ B_{\mathbf{u}}(\mathbf{y}_j) &= p_{\mathbf{u}}(\mathbf{y}_j, \mathbf{D}_j, \mathcal{Y}_{j-1})(1 - p_{\mathbf{u}}(\mathbf{y}_j, \mathbf{D}_j, \mathcal{Y}_{j-1})), \end{aligned} \quad (7)$$

where $B_{\mathbf{u}}(\mathbf{y}_j)$ is the conditional Bernoulli variance for outcome \mathbf{y}_j of data in design \mathbf{D}_j , and the conditional probability of an excursion is

$$p_{\mathbf{u}}(\mathbf{y}_j, \mathbf{D}_j, \mathcal{Y}_{j-1}) = P(\xi_{\mathbf{u}} \leq t | \mathbf{y}_j, \mathcal{Y}_{j-1}; \mathbf{D}_j). \quad (8)$$

¹⁷¹ The notation in Equation (7) indicates that the EIBV is an expectation with respect to the random
¹⁷² data \mathbf{y}_j for design \mathbf{D}_j , conditional on the history of sampling results \mathcal{Y}_{j-1} .

The criterion for selecting design \mathbf{D}_j and then getting data \mathbf{y}_j at stage $j = 1, \dots, J$, is based on the minimum EIBV computed for all designs in a candidate waypoint set denoted \mathcal{D}_j . We have

$$\mathbf{D}_j = \operatorname{argmin}_{\mathbf{D}'_j \in \mathcal{D}_j} \text{EIBV}(\mathbf{D}'_j). \quad (9)$$

¹⁷³ Using expressions similar to that of [29], the EIBV in Equation (7) can be evaluated in closed
¹⁷⁴ form. Denoting the variance reduction from data by $\mathbf{V}_j = \mathbf{G}_j \mathbf{F}_j \mathbf{S}_{j-1}$, see Equation (3), the
¹⁷⁵ EIBV becomes

$$\begin{aligned} \text{EIBV}(\mathbf{D}'_j) &= \sum_{i=1}^n \text{EBV}_{\mathbf{u}_i}(\mathbf{D}'_j) \\ \text{EBV}_{\mathbf{u}_i}(\mathbf{D}'_j) &= \Phi_2 \left(\begin{bmatrix} t \\ -t \end{bmatrix}; \begin{bmatrix} m_{j-1}(i) \\ -m_{j-1}(i) \end{bmatrix}, \mathbf{W}_j(i, i) \right), \end{aligned} \quad (10)$$

with,

$$\mathbf{W}_j(i, i) = \begin{bmatrix} T(i, i) & -V_j(i, i) \\ -V_j(i, i) & T(i, i) \end{bmatrix}, \quad T(i, i) = S_{j-1}(i, i) + V_j(i, i).$$

¹⁷⁶ We next give some intuition for this EIBV criterion. Fig. 4 illustrates a Gaussian PDF (left)
¹⁷⁷ representing the current knowledge about salinity at some location. In this case it is standardized
so that $Z_1 = \frac{\xi_{u_i} - m_{j-1}(i)}{\sqrt{S_{j-1}(i,i)}}$ for location u_i . The scaled threshold $t - m_{j-1}(i)$ is shown as a vertical

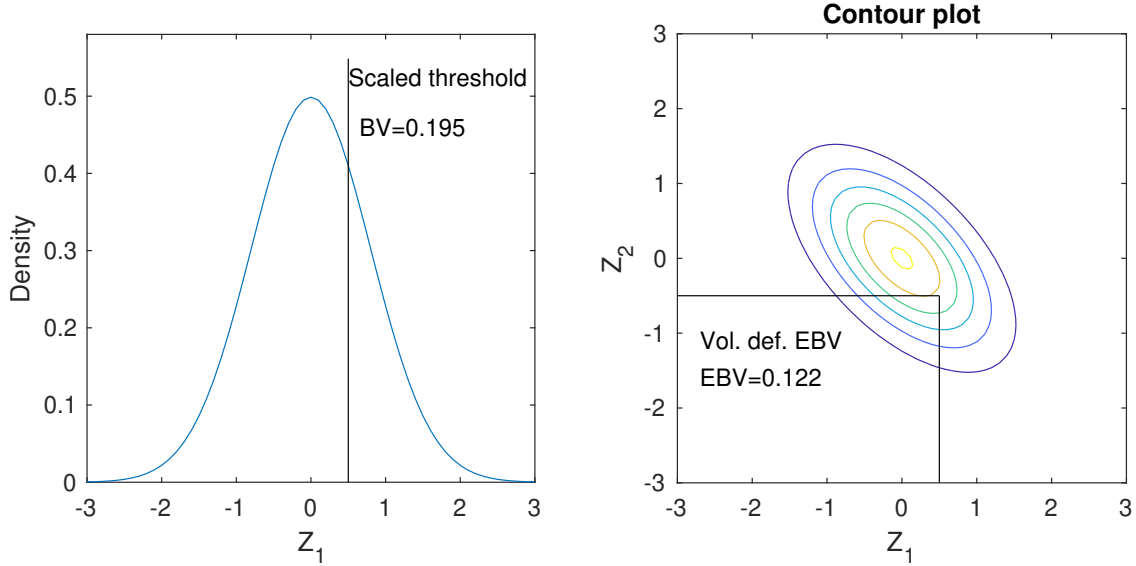


Fig. 4: Left: The density curve represents the current knowledge at a selected location, while the vertical line indicates the threshold. The Bernoulli variance (BV) is indicated. Right: The EBV calculation involves bivariate Gaussian cumulative probabilities, which is the volume below the contours in the bottom left region.

¹⁷⁸
¹⁷⁹ line. With variance $s_{j-1}^2(i) = S_{j-1}(i,i)$, the current $\text{BV} = p(1-p)$, $p = \Phi(\xi_{u_i}; m_{j-1}(i), s_{j-1}^2(i))$
¹⁸⁰ is also displayed.

¹⁸¹ We can collect data and get more information. The expected BV (EBV) at this location is then
¹⁸² available as a cumulative probability as indicated in Fig. 4 (right). Assume next that the mean at
¹⁸³ another location is lower, meaning that the threshold $t - m_{j-1}(i)$ moves to the right in the left
¹⁸⁴ display. Then the BV decreases, and the EBV illustrated in the right display also decreases as
¹⁸⁵ the vertical line moves right and the horizontal line moves down. The EBV is further smallest
¹⁸⁶ when there is much negative correlation in the density in Fig. 4 (right). From matrix $\mathbf{W}_j(i,i)$
¹⁸⁷ in Equation (11), we see that this occurs when the variance reduction $V_j(i,i)$ is large compared
¹⁸⁸ with $S_{j-1}(i,i) + V_j(i,i)$.

¹⁸⁹ Previous research has demonstrated the possibility of using EIBV as the design criterion for
¹⁹⁰ AUV adaptive sampling in two-dimensional domains [15]. We next explain how we build on

191 this to construct effective AUV operations in 3D adaptive sampling plans.

192 **IV. PATH PLANNING ALGORITHM**

193 **A. Adaptive sampling**

194 The GRF model updating in Equation (3) and closed form EIBV calculation in Equation (10)
enable adaptive AUV sampling. We summarize the approach in Algorithm 1,

Algorithm 1 Informative myopic sampling algorithm

Initialization: $\mathbf{m}_0, \mathbf{S}_0, t, \mathcal{Y}_0 = \emptyset, \mathcal{D}_1$

$j = 1$

while $j \leq N_{steps}$ **do**

Plan: Evaluate EIBV(\mathbf{D}'_j) for all $\mathbf{D}'_j \in \mathcal{D}_j$ ▷ Eq. (7) and (10)

$\mathbf{D}_j = \operatorname{argmin}_{\mathbf{D}'_j \in \mathcal{D}_j} \text{EIBV}(\mathbf{D}'_j)$ ▷ Eq. (9)

Go to design \mathbf{D}_j with the AUV, set design matrix \mathbf{F}_j , form set \mathcal{D}_{j+1} .

Sense: Gather in-situ AUV data \mathbf{y}_j according to design \mathbf{D}_j .

$\mathcal{Y}_j = (\mathcal{Y}_{j-1}, \mathbf{y}_j)$.

Update : $\mathbf{G}_j = \mathbf{S}_{j-1} \mathbf{F}_j^T (\mathbf{F}_j \mathbf{S}_{j-1} \mathbf{F}_j^T + \mathbf{R}_j)^{-1}$

$\mathbf{m}_j = \mathbf{m}_{j-1} + \mathbf{G}_j (\mathbf{y}_j - \mathbf{F}_j \mathbf{m}_{j-1}), \mathbf{S}_j = \mathbf{S}_{j-1} - \mathbf{G}_j \mathbf{F}_j \mathbf{S}_{j-1}$ ▷ Eq. (3)

$j = j + 1$

end while

195

196 Note that as outlined this defines a myopic or greedy approach to adaptive sampling. This is
197 not necessarily optimal. The myopic evaluation is done by taking the expectation of data at this
198 stage only, without anticipation of what future sampling efforts might bring. The optimal solution
199 to the sequential sampling design problem would also account for the sampling efforts at future
200 stages. However, from the mathematical and computational setting, it is not feasible to find the
201 optimal design strategy because it involves combinatorial growth of possible paths requiring
202 intermixed optimization and expected values. Instead, one often resorts to the outlined myopic
203 strategy. More nuanced approaches exist for doing longer-horizon search, for instance variants of
204 Markov Decision Processes (MDPs) or partially observed MDPs [30], rapidly-exploring random
205 trees [31] or those based on genetic algorithms [32]. Such approaches will typically perform
206 better than the myopic heuristic in situations with forbidden regions or with high collision risks,

²⁰⁷ but it is not easy to use these in large-scale computations onboard the AUV. Further, restricted
²⁰⁸ Monte Carlo search or pruning of paths, these non-myopic approaches will not necessarily
²⁰⁹ improve performance compared with a myopic search on the regular waypoint graph case [15].
²¹⁰ We will limit scope to the myopic calculations (Algorithm 1) in this work.

²¹¹ For the 3D application we consider here, the sequential sampling is restricted to a path
²¹² embedded on a predefined grid of waypoints. In practice, the EIBV is computed for a set of
²¹³ neighborhood waypoint locations, meaning that the candidate design \mathbf{D}'_j must be among those
²¹⁴ possible designs defining \mathcal{D}_j .

²¹⁵ For small AUVs and large field, it might be possible to move the AUV where ever it needs
²¹⁶ to be. However, this might lead to an excess of manoeuvring time for the operation. To foster
²¹⁷ the efficiency of the autonomous sampling process, a smooth-filtering method is applied to
²¹⁸ achieve AUV-friendly path planning (Algorithm 2). It firstly selects neighboring locations, and
²¹⁹ two vectors will be formed. Vector \vec{b}_1 is defined from the previous location to the current location,
²²⁰ whereas vector \vec{b}_2 is from the current location to the potential candidate locations. Next, the inner
²²¹ products between these two vectors is calculated, and only candidate locations with positive inner
products will be considered for EIBV evaluation.

Algorithm 2 Smooth-filtering algorithm

Require: $\mathbf{D}_{j-1}, \mathbf{D}_{j-2}$

$$D^* = \{\mathbf{u} \in \mathcal{M} \text{ such that } |\mathbf{u} - \mathbf{D}_{j-1}| < \text{neighboring distance}\}$$

$$\vec{b}_1 = \mathbf{D}_{j-1} - \mathbf{D}_{j-2}$$

$$i = 1$$

while $i \leq N_{D^*}$ **do**

$$\vec{b}_2 = \mathbf{D}_i^* - \mathbf{D}_{j-1}$$

if $\vec{b}_1 \cdot \vec{b}_2 < 0$ **then**

 Abandon \mathbf{D}_i^* .

end if

$$i = i + 1$$

end while

$$\mathbf{D}_j = D^*$$

²²²

²²³ A map view version of the smooth-filtering is depicted on a 2D waypoint graph in Fig. 5.
²²⁴ In 3D, the principle is the same, except that it is expanded to include the vertical candidate

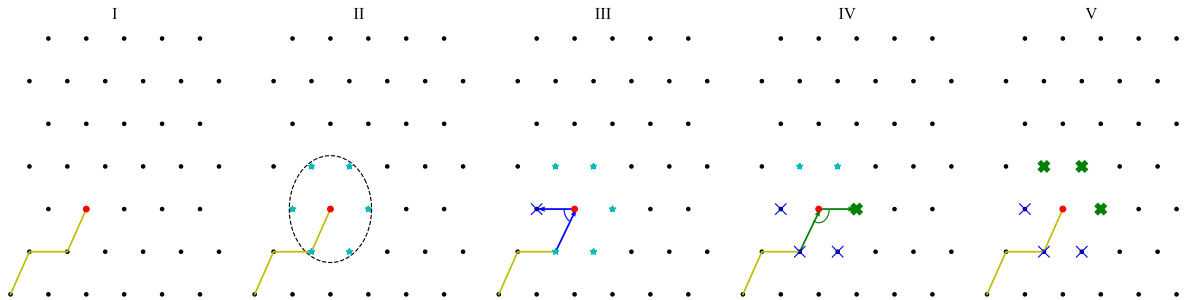


Fig. 5: Smooth path planning. I: arrive at the current location; II: search all neighboring locations; III, IV: compute inner products; V: select qualified candidate locations. Blue thin crosses indicate the abandoned locations, whereas the green thick crosses indicate the filtered locations.

locations as well. This path smooth-filtering algorithm is effective since it removes locations which might require a hydrodynamic maneuver to go there [33]. The smooth-filtered trajectory further avoids time-consuming turning which would increase the traveling time and introduce location inaccuracy.

229 V. SIMULATION STUDY

To compare the performance between some existing algorithms and the 3D myopic algorithm that we have developed here, a simulation study is conducted. We next describe the case, present the various methods and discuss results.

233 A. Simulation setup

We use data from the numerical ocean model SINMOD as a reference for specifying realistic trends and variabilities for the oceanographic fjord-river water masses. Fig. 6 shows the average surface salinity field predicted for the first week in May using SINMOD. Four outlets from the river are recognized. The salinity variation from the river mouth to the ocean changes dramatically from bins of [0, 3] to [28, 30] ppt. The boundary between the freshwater and the more saline fjord water is clearly depicted by the contours.

To narrow down the focus on mapping the front of the river plume in 3D, a smaller region of interest in the easternmost part is selected (see blue rectangle in Fig. 6). Five depth layers 0.5m, 1.0m, 1.5m, 2.0m, 2.5m are used.

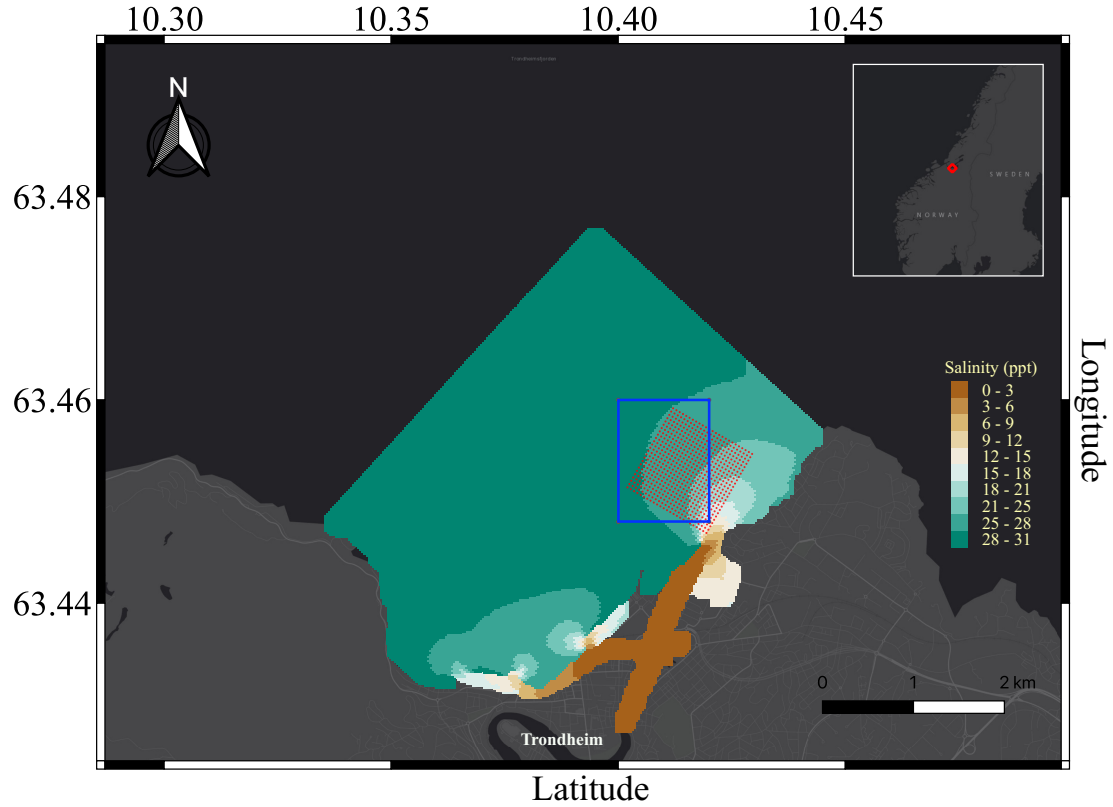


Fig. 6: Regional average surface salinity prediction in May 2021 from SINMOD. The blue rectangle indicates the designated simulation area (Section V), and the red dotted regions indicate the waypoint graph used in the field deployment (Section VI). The grid consists of 25×25 nodes in each lateral axis and 5 layers in depth. *Courtesy of SINTEF Ocean and ESRI basemap.*

A 3D GRF benchmark field is created based on the data extracted from SINMOD on the desired simulation region. The mean values are set from averaging SINMOD data. The coefficients used in the Matérn covariance kernel are specified as $\sigma = 0.71$, $\phi_1 = 0.008$, $\phi_2 = 2.25$ and $r = 0.2$.

Fig. 7 shows one realization from our GRF model with the specified mean and covariance model. This is regarded as the ground truth in the simulation. There is clearly river plume areas to the south-east and near the surface, and realistic variability in salinity extent with some mixing of water masses, indicating that the GRF model emulates the physical phenomenon rather well.

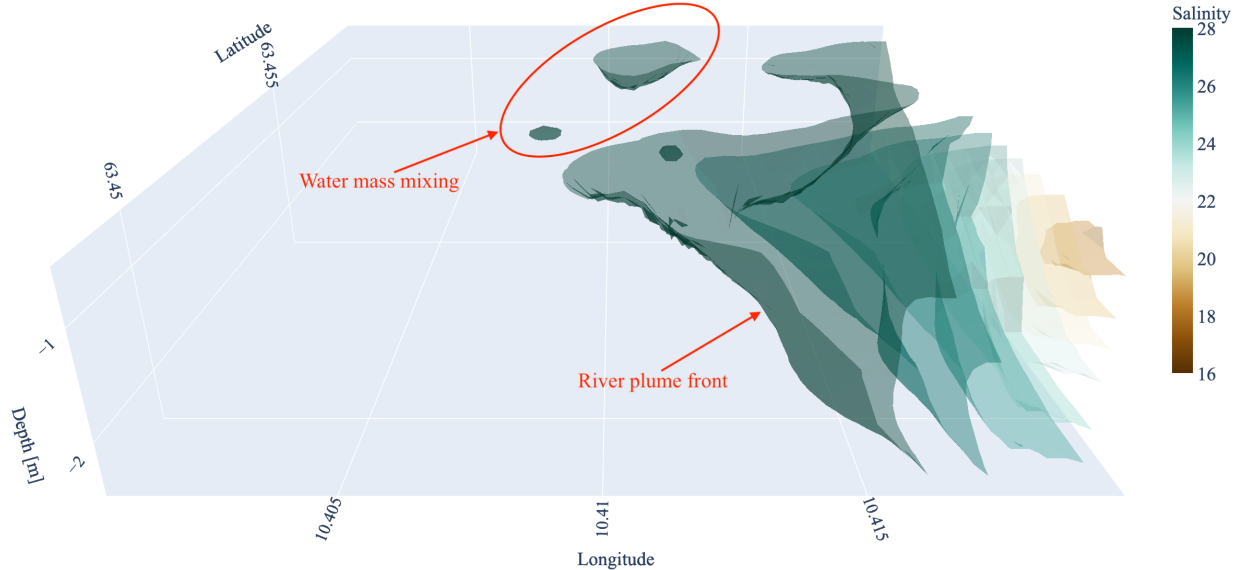


Fig. 7: One benchmark salinity field used in the simulation study. Some water blobs are shown on the north side of the region.

252 **B. Simulation approaches**

253 We next describe two additional sampling strategies that are compared with our suggested 3D
 254 adaptive sampling method. In all three, the GRF proxy model provides an easy way to update
 255 the knowledge of the field by measuring the data at specified locations. The differences occur
 256 in how the data is included in the on-board computing and in what sampling strategy is used to
 257 explore the domain. When we compare results of the various approaches, they will be influenced
 258 by the sampling methodology used.

259 *1) Adaptive Myopic 2D:* For the adaptive myopic 2D, the AUV is only moving adaptively in
 260 the middle layer with the myopic strategy. It updates the entire field based on the data obtained
 261 from the middle layer at 1.5m depth. In practice, the AUV needs to calibrate its navigational
 262 errors by constantly popping up onto the surface and request accurate GPS locations and dive
 263 back to the place where it should continue. This is achieved by a yoyo pattern, as shown in
 264 Fig. 8.

265 *2) Non-adaptive lawnmower:* For the non-adaptive lawnmower, Fig. 9 shows that the AUV
 266 will follow a pre-designed 3D lawnmower pattern. In the lateral direction, the surface-projected
 267 trajectory will be a typical lawnmower manoeuvre. To extend it into 3D, a vertical yoyo manoeuvre
 268 is added in addition to the lateral lawnmower. This pre-programmed method requires no statistical

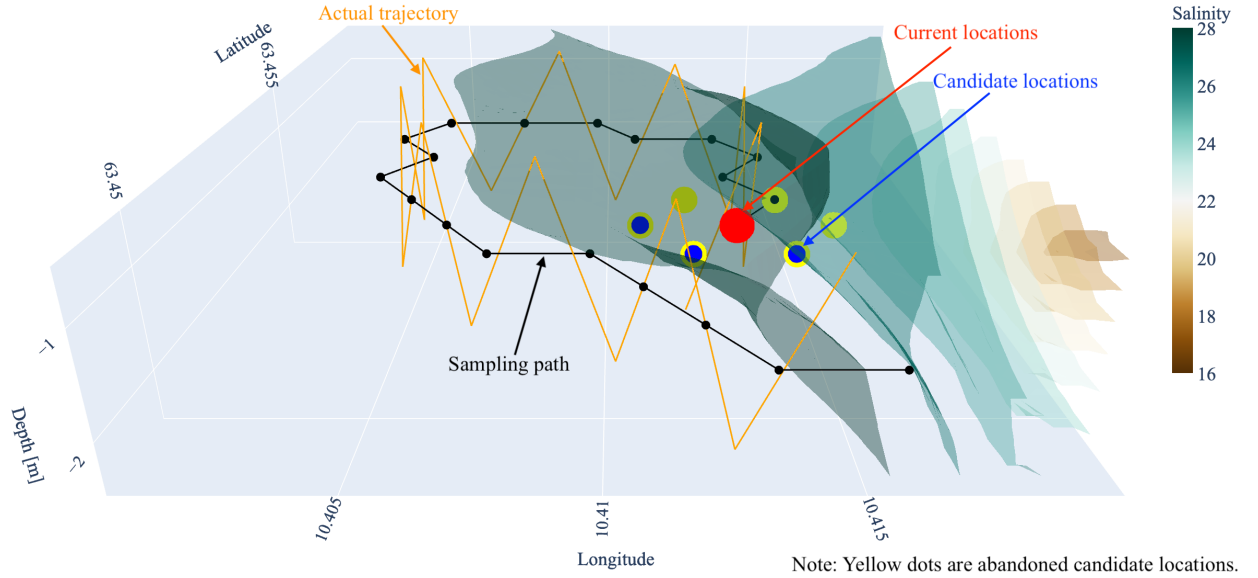


Fig. 8: Adaptive myopic 2D algorithm illustration. The outmost envelope shows the estimated boundary after sampling 20 locations. Note that the yoyo pattern is shown as an illustration. It can be denser in the actual setting.

computations at waypoints, and it uncovers the field with large coverage. But the approach is usually time-consuming and inefficient in finding interesting features as it does not adapt to the data.

3) Adaptive Myopic 3D: Our suggested adaptive myopic 3D strategy extends the potential candidate sampling locations from one layer to include multiple layers. Therefore, it adapts to the field data with a much wider perspective. It is further both energy-efficient and time-efficient. One example of the adaptive 3D myopic path planning is depicted in Fig. 10. One can see that at each stage, candidate locations will be generated in three dimensions. Only a few (shown as blue in Fig. 10) will be selected for the EIBV calculation due to the constraints of AUV maneuverability.

279 C. Simulation results and discussion

280 Fig. 8~10 show how each strategy behaves for one specific generated salinity field. To remove
 281 random effects, results of 100 replicate simulation results are averaged and shown in Fig. 11.
 282 At each time step of the runs, IBV (Integrated Bernoulli Variance), RMSE (Root Mean Squared

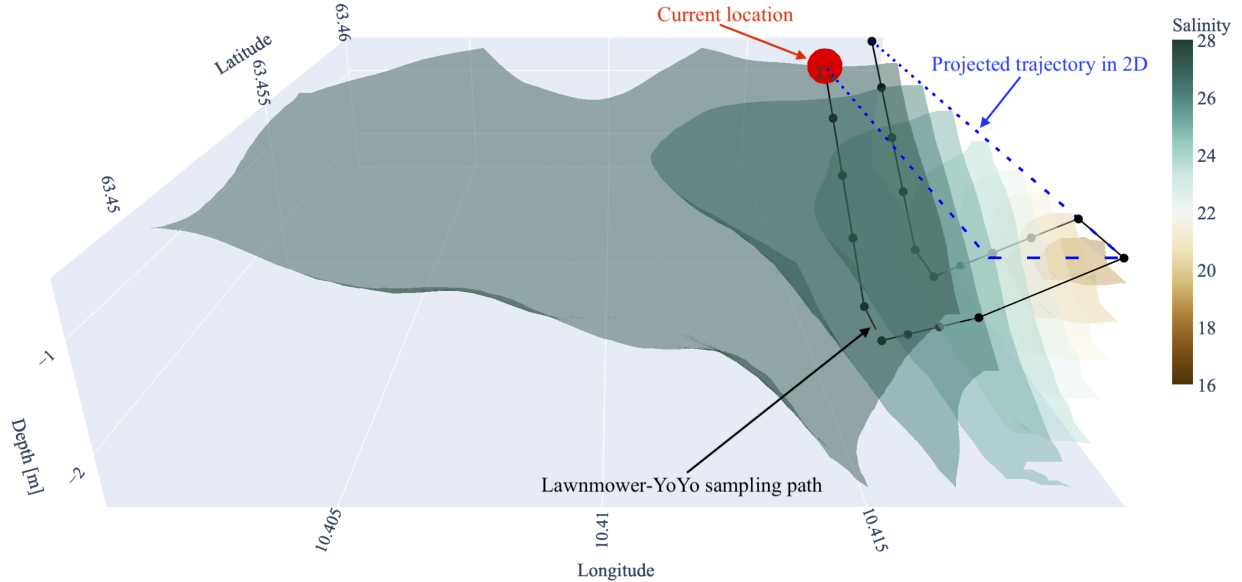


Fig. 9: Lawnmower-yoyo maneuver illustration. The estimated boundary after observing 20 sampling locations is shown as the outermost envelope.

283 Error), Variance reduction and Distance traveled are monitored for comparison of the three
284 strategies.

285 The IBV indicator shows that the Lawnmower-yoyo pattern has the slowest reduction of the
286 three strategies. However, it goes down quickly when the robot is in the area of interest, i.e.,
287 the boundary region or the front of the river plume, performing better than Myopic 2D after
288 about 15 iterations (The same holds for RMSE and Variance reduction.) This occurs because the
289 lawn mower strategy can get lucky and the AUV runs into interesting parts of the domain, but
290 it can also miss this entirely in the given time window. Even though the Myopic 3D strategy is
291 guided by EIBV reduction, it also achieves large reduction in RMSE and variance, and more so
292 than the other methods. It performs better than the 3D Lawnmower strategy because it explores
293 new parts of the domains and in doing so avoids locations that are highly correlated to the ones
294 already sampled.

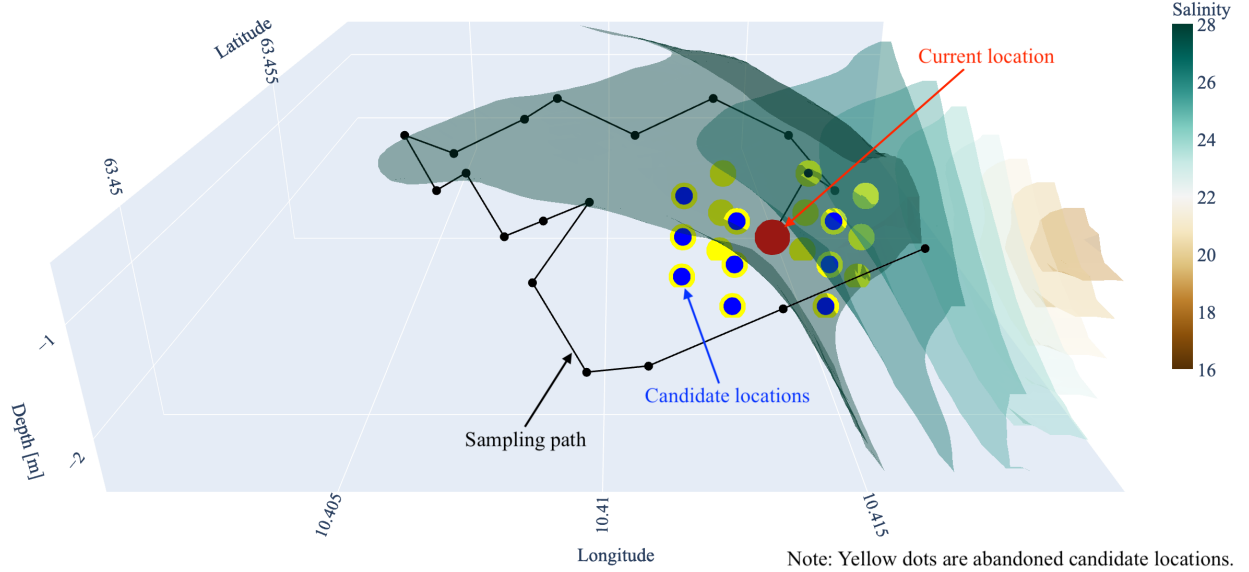


Fig. 10: Adaptive myopic 3D sampling illustration. The outermost envelope shows the estimated river plume front after sampling 20 locations with the adaptive myopic 3D path planning.

With the same starting location and about the same traveled distance (Fig. 11, lower right), the 3D version of the myopic planning reveals the most information of the field within the three strategies. The flexibility in 3D enables the AUV to both explore and exploit the environment effectively.

VI. AUV EXPERIMENTS IN THE NIDELVA PLUME

We next describe and show results of AUV experiments done in late Spring 2021 to map the Nidelva river plume, Trondheim, Norway. The adaptive AUV experiments were conducted on July 6th 2021. Before that, we gathered various complementary data. The phone footage on May 27th shows a visible river plume (Fig. 12). A satellite image on June 2nd (Fig. 13) shows how the river plume area is unfolded by pollen flushed away by the river in the spring season. That matches very well with the phone footage (Fig. 12). Such data motivates AUV sampling for calibration, improved resolution and 3D characterization.

A. Experiment setup

1) *Discretize the grid:* Computational constraints and practical matters lead to a $25 \times 25 \times 5$ grid discretization within the $1\text{km} \times 1\text{km} \times 2\text{m}$ box region overlapping the river plume area as

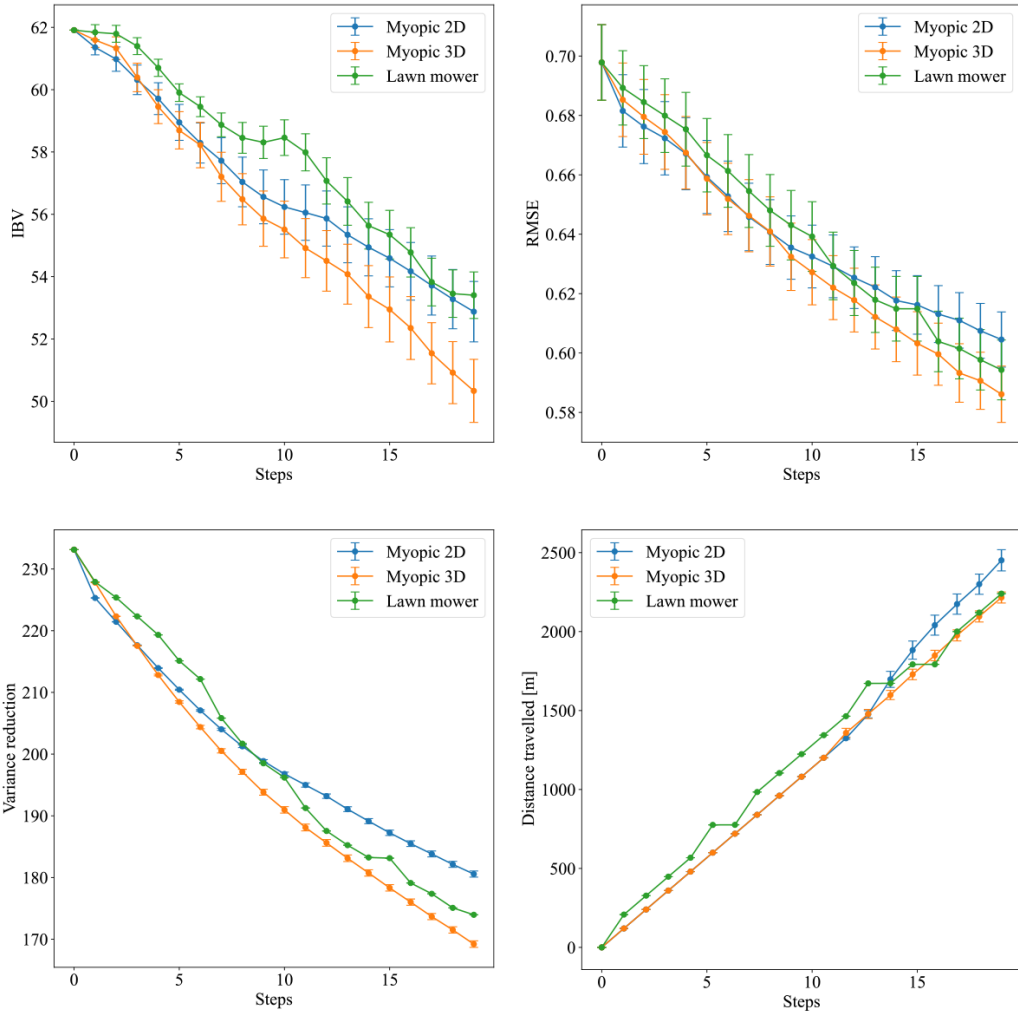


Fig. 11: Average results from 100 replicate simulations for 20 sampling locations. The standard error is depicted as vertical lines.

310 shown in Fig. 6 (red dots). We concentrate our effort on the near-surface regions (depth smaller
 311 than 2.5m) because ocean model data and observations made during an initial AUV transect
 312 (Fig. 14) show that the freshwater river plume tends to float close to the surface regions [1].

313 *2) Building the prior:* To form a prior, we use SINMOD data as a core building block. First,
 314 we allocate mean values to each 3D grid node, extracted from averages over many SINMOD

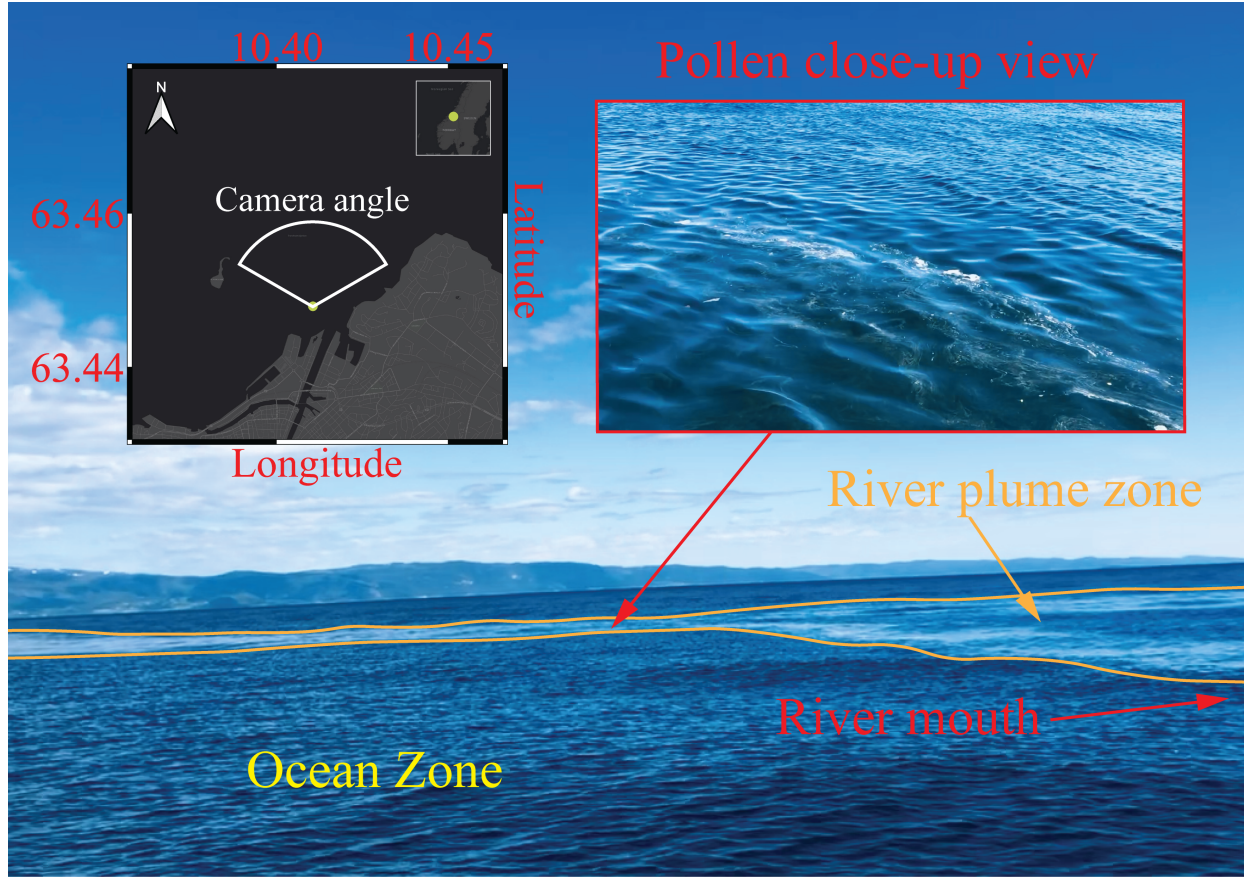
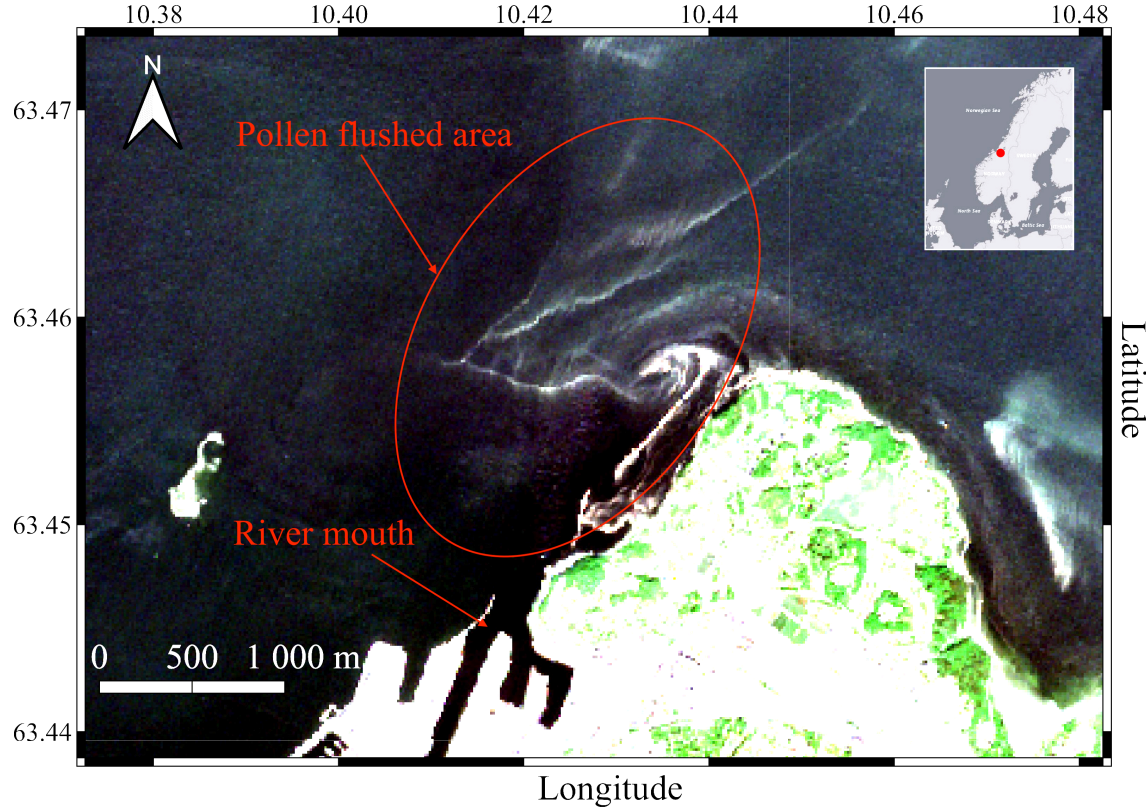


Fig. 12: River plume zone captured by the mobile phone on May 27th 2021. The camera perspective is shown as the white fan on the left corner which indicates the area where the plume occurs.

315 runs. Second, we calibrate these mean values in a regression model using AUV data from a
 316 preliminary transect survey. A linear regression model $y_{\mathbf{u}_k} = \beta_0 + \beta_1 y_{\mathbf{u}_k}^{\text{SINMOD}}$ is fitted, where
 317 \mathbf{u}_k indicate locations of transect line AUV data $y_{\mathbf{u}_k}$ and SINMOD data $y_{\mathbf{u}_k}^{\text{SINMOD}}$. The fitted
 318 coefficients $\hat{\beta}_0$, $\hat{\beta}_1$ adjust the entire field, and $\hat{\beta}_0 + \hat{\beta}_1 y_{\mathbf{u}_k}^{\text{SINMOD}}$ provides the prior mean in the
 319 onboard model used in the AUV deployment.

320 The coefficients for the Matérn kernel are approximated using empirical variograms of the
 321 AUV data collected from the initial survey. They are specified to $\sigma = 2$, $\phi_1 = 0.011$, $\phi_2 = 0.94$
 322 and $r = 0.55$. Careful assessment of these parameters is important when it comes to sharpening
 323 the performance of the adaptive sampling algorithm such that it recognizes the boundary more
 324 agilely. However, further tweaking of these parameters are out of the scope of this work.



Satellite image captured by Sentinel-2 on June-2nd 2021, courtesy of Copernicus Sentinel data [2021]

Fig. 13: Satellite image captured on 2 June 2021, showing the visible river plume thanks to the pollen flushed away by the river.

325 3) *AUV deployment*: LAUV Roald (Fig. 15) from the Applied Underwater Robotics Laboratory
 326 at NTNU was employed in the Nidelva missions. All the essential scripts were integrated onboard
 327 on the backseat NVIDIA Jetson TX2 CPU. For hardware and software in the loop testing and
 328 the actual deployment we relied on the framework developed by [12]. The implementation
 329 of Algorithm 1 and 2 requires Robot Operating Systems (ROS) [34] and a software bridge
 330 to the LAUV, running DUNE (DUNE :Unified Navigation Environment [35]) embedded and
 331 communicating over the Inter Module Communication (IMC) message protocol [36].

332 The software bridge between ROS and IMC was adapted from the Swedish Maritime Robotics
 333 Centers implementation of a ROS-IMC bridge [37]¹ to include messages going from ROS to the
 334 vehicle. In addition, a wrapper for the vehicle IMC messages was used, enabling easy interaction

¹https://github.com/smarc-project/imc_ros_bridge

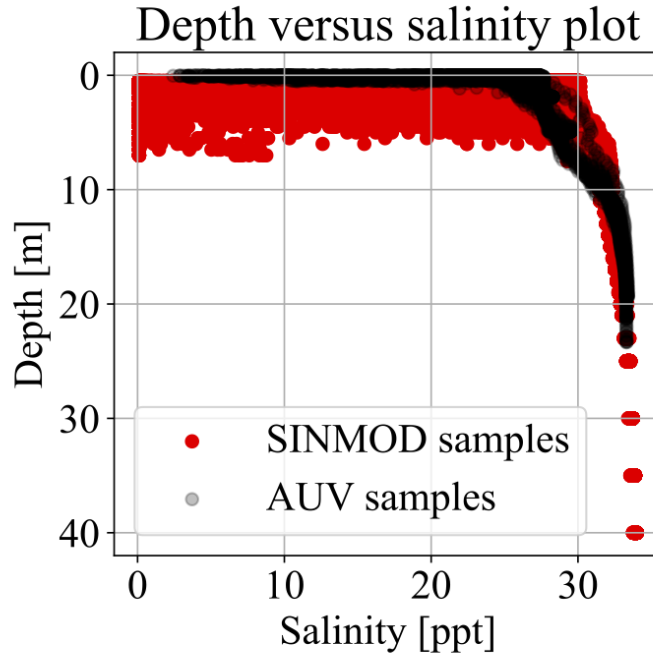


Fig. 14: Salinity versus depth plot from AUV in-situ measurements and from SINMOD prediction. Both SINMOD and the in-situ measurements show that most salinity variation happens close to the surface.

335 between the adaptive software and the vehicle. The communication bridge and framework
 336 between ROS and IMC use the same back-seat interface as [16], with IMC messages being
 337 transmitted over Transmission Control Protocol (TCP) [38] between the main CPU and the
 338 auxiliary CPU in the AUV. The adaptive code is run in the auxiliary CPU in order to preserve the
 339 integrity of the main CPU. For illustration, a flowchart containing the main software components
 340 is presented in Fig. 16.

341 *B. Experiment results and discussion*

342 Fig. 17 shows the posterior EPs after assimilating all the AUV measurements from the adaptive
 343 mission. When the EP is close to 1, it is classified as river water, while ocean water has
 344 probabilities close to 0. Some parts of the domain are still unexplored and have intermediate
 345 probabilities. In its adaptive sampling efforts to distinguish the water masses, the AUV travels
 346 between different layers and traverse the lateral domain. The sampling mainly takes place in the



Fig. 15: LAUV Roald is taking a shower after the heavy duty.

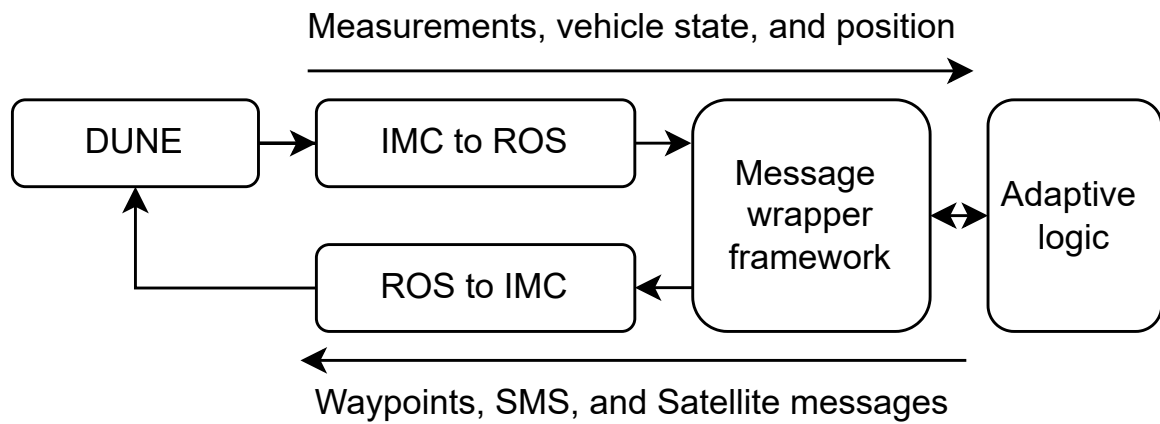


Fig. 16: Main software components in the communication between the adaptive code and the vehicle. DUNE [35] is running on the main CPU of the AUV while the IMC [36] messages are transmitted via TCP [38] to an auxiliary CPU, where ROS [34] and the adaptive code is run.

Posterior field after AUV sampling

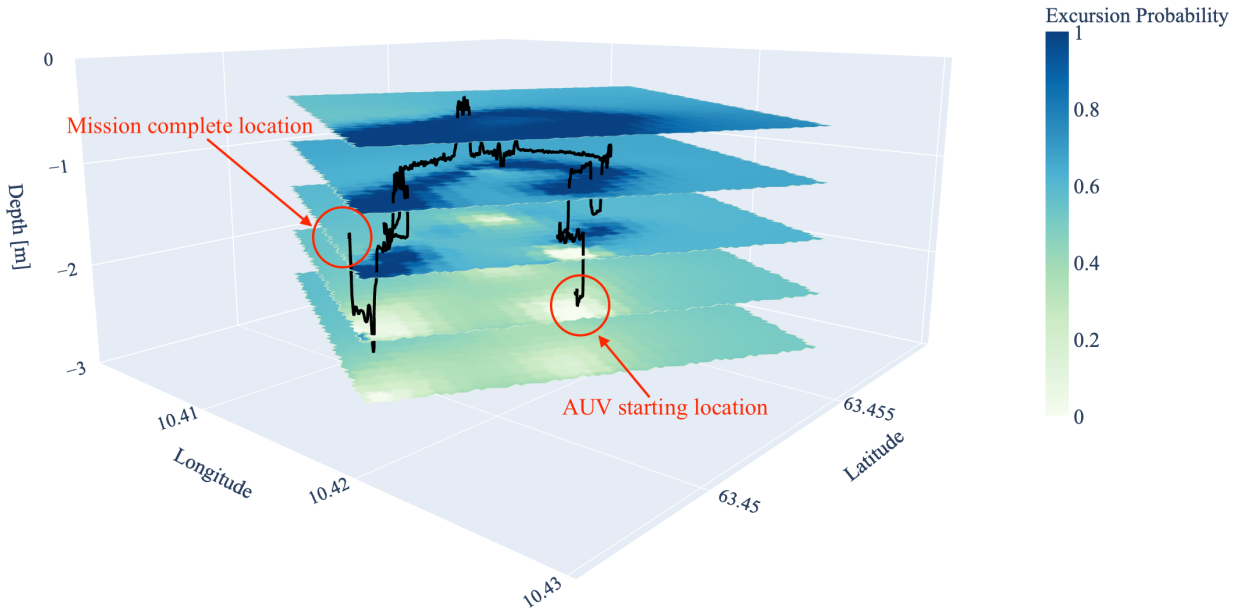


Fig. 17: Excursion probability for the posterior field. It describes how similar the water mass is to the river water. Values near 1 (blue) represents river water, while 0 (white) represents ocean water.

347 top three layers that mirrors the buoyant river plume assumption, but it dips down to 2m and
 348 2.5m. The adaptive behavior guides the agent to be within the boundary region instead of putting
 349 too much effort on either side of the front. According to the updated field, there appears to be
 350 patches of river waters going down to 1m and 1.5m, but most river water is near the surface.

351 In Fig. 18 we compare prior and posterior EPs for the top two layers. Clearly, the AUV
 352 reveals a bigger plume region than what is predicted by the SINMOD prior model. At 1.0 m
 353 there appears to be water mass separation. This kind of separation is likely very heterogeneous
 354 in space and time, and the displayed results only show predicted conditions at the day of the
 355 mission.

356

VII. CONCLUSION

357 The main contribution of this work is to apply Gaussian random field models for three-
 358 dimensional north-east-down domains in the context of adaptive sampling with real-time computation
 359 and maneuverability routines on a robotic vehicle. The adaptive sampling routine presented here

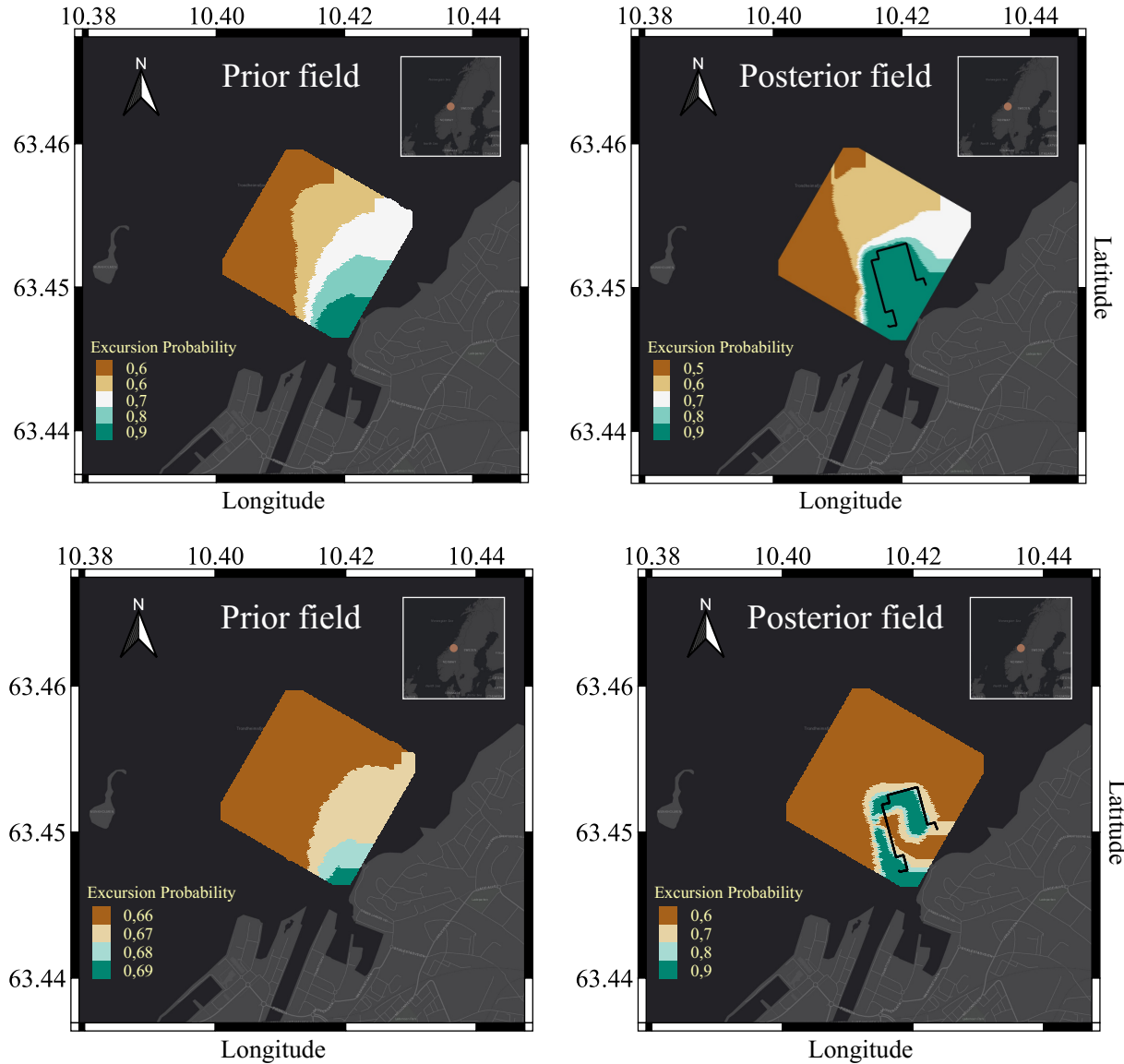


Fig. 18: Excursion probability comparison for the prior field (left) and the posterior field (right) at 0.5 m depth (top) and 1.0 m depth (bottom). The AUV trajectory is shown as the black line in the right column.

is tailored to frontal systems, and it relies on reduction of the expected integrated Bernoulli variance. We conducted a simulation study comparing the suggested approach with more standard approaches. Results demonstrate the capability of the adaptive myopic three dimensional sampling in a field deployment. The AUV managed to distinguish the different water masses in a river plume in a Norwegian fjord-river system.

365 River plumes are influenced by many factors such as winds, waves and tides, and we could
 366 likely model statistical correlations more sensibly by using a non-stationary Gaussian random
 367 field prior [39]. Our method uses ocean model data to build a reasonable prior model of the
 368 salinity field in 3D. However, when this type of information is lacking, the prior belief can also
 369 be constructed based on other data, possibly satellite imagery or buoy information. As AUV data
 370 are rather sparse, there is likely much to gain by using spatially covering physical modeling data
 371 and satellite data, as this allows a better initial model for sampling.

372 The time variation will play an important role if the AUV deployment lasts longer. This is
 373 naturally the case when the frontal region gets bigger and the distance traveled by the AUV
 374 increases. In long-term deployments it will also be important to capture the temporal effect [25].
 375 The current myopic philosophy works well for a small river plume. As the plume gets bigger, or
 376 one has interest in capturing sub-regional plumes, there is likely some gain by using strategies that
 377 anticipate many stages [31, 32] or use the ocean physics for the three dimensional navigation [40].
 378 Other opportunities stem from using adaptive sampling in a cooperative fleet as discussed in [41].

379 ACKNOWLEDGMENT

380 We acknowledge support from Norwegian Research Council (RCN) through the MASCOT
 381 project 305445. The authors thank AURLab NTNU for the support, collaboration, and easy
 382 access to testing equipment. We thank Kay Arne Skarpnes for his help during all the field-trials
 383 in 2021. We thank SINTEF Ocean for supplying SINMOD data.

384 REFERENCES

- 385 [1] A. R. Horner-Devine, R. D. Hetland, and D. G. MacDonald, “Mixing and transport in
 386 coastal river plumes,” *Annual Review of Fluid Mechanics*, vol. 47, no. 1, pp. 569–594,
 387 2015.
- 388 [2] S. Constantin, D. Doxaran, and S. Constantinescu, “Estimation of water turbidity and
 389 analysis of its spatio-temporal variability in the danube river plume (black sea) using modis
 390 satellite data,” *Continental Shelf Research*, vol. 112, pp. 14–30, 2016.
- 391 [3] A. A. Osadchiev and P. O. Zavialov, “Lagrangian model of a surface-advection river plume,”
 392 *Continental Shelf Research*, vol. 58, pp. 96–106, 2013.

- [4] S. Zheng, W. Guan, S. Cai, X. Wei, and D. Huang, “A model study of the effects of river discharges and interannual variation of winds on the plume front in winter in pearl river estuary,” *Continental Shelf Research*, vol. 73, pp. 31–40, 2014.
- [5] F. M. Falcieri, A. Benetazzo, M. Sclavo, A. Russo, and S. Carniel, “Po river plume pattern variability investigated from model data,” *Continental Shelf Research*, vol. 87, pp. 84–95, 2014.
- [6] R. Mendes, N. Vaz, D. Fernández-Nóvoa, J. Da Silva, M. Decastro, M. Gómez-Gesteira, and J. Dias, “Observation of a turbid plume using modis imagery: The case of douro estuary (portugal),” *Remote sensing of environment*, vol. 154, pp. 127–138, 2014.
- [7] G. S. Saldías, J. L. Largier, R. Mendes, I. Pérez-Santos, C. A. Vargas, and M. Sobarzo, “Satellite-measured interannual variability of turbid river plumes off central-southern chile: Spatial patterns and the influence of climate variability,” *Progress in Oceanography*, vol. 146, pp. 212–222, 2016.
- [8] E. Park and E. M. Latrubesse, “Modeling suspended sediment distribution patterns of the amazon river using modis data,” *Remote Sensing of Environment*, vol. 147, pp. 232–242, 2014.
- [9] J. Hwang, N. Bose, and S. Fan, “Auv adaptive sampling methods: A review,” *Applied Sciences*, vol. 9, no. 15, p. 3145, 2019.
- [10] E. Fiorelli, N. E. Leonard, P. Bhatta, D. A. Paley, R. Bachmayer, and D. M. Fratantoni, “Multi-auv control and adaptive sampling in monterey bay,” *IEEE Journal of Oceanic Engineering*, vol. 31, no. 4, pp. 935–948, 2006.
- [11] T. O. Fossum, G. M. Fragoso, E. J. Davies, J. E. Ullgren, R. Mendes, G. Johnsen, I. Ellingsen, J. Eidsvik, M. Ludvigsen, and K. Rajan, “Toward adaptive robotic sampling of phytoplankton in the coastal ocean,” *Science Robotics*, vol. 4, no. 27, p. eaav3041, 2019.
- [12] T. Mo-Bjørkelund, T. O. Fossum, P. Norgren, and M. Ludvigsen, “Hexagonal grid graph as a basis for adaptive sampling of ocean gradients using auvs,” in *Global Oceans 2020: Singapore – U.S. Gulf Coast*, 2020, pp. 1–5.
- [13] P. Rogowski, E. Terrill, and J. Chen, “Observations of the frontal region of a buoyant river plume using an autonomous underwater vehicle,” *Journal of Geophysical Research: Oceans*, vol. 119, no. 11, pp. 7549–7567, 2014.
- [14] Y. Zhang, J. G. Bellingham, J. P. Ryan, B. Kieft, and M. J. Stanway, “Autonomous four-dimensional mapping and tracking of a coastal upwelling front by an autonomous

- underwater vehicle,” *Journal of Field Robotics*, vol. 33, no. 1, pp. 67–81, 2016.
- [15] T. O. Fossum, C. Travelletti, J. Eidsvik, D. Ginsbourger, and K. Rajan, “Learning excursion sets of vector-valued gaussian random fields for autonomous ocean sampling,” *Annals of Applied Statistics*, vol. 15, no. 2, pp. 597–618, 2021.
- [16] J. Pinto, R. Mendes, J. C. B. da Silva, J. M. Dias, and J. B. de Sousa, “Multiple autonomous vehicles applied to plume detection and tracking,” in *2018 OCEANS - MTS/IEEE Kobe Techno-Oceans (OTO)*, May 2018, pp. 1–6.
- [17] R. Cui, Y. Li, and W. Yan, “Mutual information-based multi-auv path planning for scalar field sampling using multidimensional rrt*,” *IEEE Transactions on Systems, Man, and Cybernetics: Systems*, vol. 46, no. 7, pp. 993–1004, 2016.
- [18] P. Stankiewicz, Y. T. Tan, and M. Kobilarov, “Adaptive sampling with an autonomous underwater vehicle in static marine environments,” *Journal of Field Robotics*, vol. 38, no. 4, pp. 572–597, 2021.
- [19] A. Sousa, L. Madureira, J. Coelho, J. Pinto, J. Pereira, J. B. Sousa, and P. Dias, “Lauv: The man-portable autonomous underwater vehicle,” *IFAC Proceedings Volumes*, vol. 45, no. 5, pp. 268–274, 2012.
- [20] D. Slagstad and T. A. McClamans, “Modeling the ecosystem dynamics of the barents sea including the marginal ice zone: I. physical and chemical oceanography,” *Journal of Marine Systems*, vol. 58, no. 1-2, pp. 1–18, 2005.
- [21] P. F. Lermusiaux, “Uncertainty estimation and prediction for interdisciplinary ocean dynamics,” *Journal of Computational Physics*, vol. 217, no. 1, pp. 176–199, 2006.
- [22] M. Lin and C. Yang, “Ocean observation technologies: A review,” *Chinese Journal of Mechanical Engineering*, vol. 33, no. 1, pp. 1–18, 2020.
- [23] S. Martin, *An introduction to ocean remote sensing*. Cambridge University Press, 2014.
- [24] F. A. Al-Wassai and N. V. Kalyankar, “Major limitations of satellite images,” 2013.
- [25] K. H. Foss, G. E. Berget, and J. Eidsvik, “Using an autonomous underwater vehicle with onboard stochastic advection-diffusion models to map excursion sets of environmental variables,” *Environmetrics*, p. e2702, 2022.
- [26] S. Kemna, O. Kroemer, and G. S. Sukhatme, “Pilot surveys for adaptive informative sampling,” in *2018 IEEE International Conference on Robotics and Automation (ICRA)*, 2018, pp. 6417–6424.
- [27] F. S. Longman, L. Mihaylova, and L. Yang, “A gaussian process regression approach for

- 457 fusion of remote sensing images for oil spill segmentation,” in *2018 21st International*
 458 *Conference on Information Fusion (FUSION)*, 2018, pp. 62–69.
- 459 [28] N. Cressie and C. K. Wikle, *Statistics for spatio-temporal data*. John Wiley & Sons, 2015.
- 460 [29] C. Chevalier, J. Bect, D. Ginsbourger, E. Vazquez, V. Picheny, and Y. Richet, “Fast parallel
 461 kriging-based stepwise uncertainty reduction with application to the identification of an
 462 excursion set,” *Technometrics*, vol. 56, no. 4, pp. 455–465, 2014.
- 463 [30] D. Silver and J. Veness, “Monte-carlo planning in large pomdps,” *Advances in neural*
 464 *information processing systems*, vol. 23, 2010.
- 465 [31] C. Xiong, H. Zhou, D. Lu, Z. Zeng, L. Lian, and C. Yu, “Rapidly-exploring adaptive
 466 sampling tree*: A sample-based path-planning algorithm for unmanned marine vehicles
 467 information gathering in variable ocean environments,” *Sensors*, vol. 20, no. 9, p. 2515,
 468 2020.
- 469 [32] M. Bresciani, F. Ruscio, S. Tani, G. Peralta, A. Timperi, E. Guerrero-Font, F. Bonin-Font,
 470 A. Caiti, and R. Costanzi, “Path planning for underwater information gathering based on
 471 genetic algorithms and data stochastic models,” *Journal of Marine Science and Engineering*,
 472 vol. 9, no. 11, p. 1183, 2021.
- 473 [33] S. Bhat, “Hydrobatics: Efficient and agile underwater robots,” Ph.D. dissertation, KTH
 474 Royal Institute of Technology, 2020.
- 475 [34] M. Quigley, “Ros: an open-source robot operating system,” in *ICRA 2009*, 2009.
- 476 [35] J. Pinto, P. S. Dias, R. Martins, J. Fortuna, E. Marques, and J. Sousa, “The lsts toolchain
 477 for networked vehicle systems,” in *2013 MTS/IEEE OCEANS - Bergen*, 2013, pp. 1–9.
- 478 [36] LSTS. (2022) Inter module communication protocol. [Online]. Available: <https://lsts.pt/docs/imc/master>
- 479
- 480 [37] S. Bhat, I. Torroba, Ö. Özkahraman, N. Bore, C. I. Sprague, Y. Xie, I. Stenius, J. Severholt,
 481 C. Ljung, J. Folkesson *et al.*, “A cyber-physical system for hydrobatic auvs: system
 482 integration and field demonstration,” in *2020 IEEE/OES Autonomous Underwater Vehicles*
 483 *Symposium (AUV)*. IEEE, 2020, pp. 1–8.
- 484 [38] V. Cerf and R. Kahn, “A protocol for packet network intercommunication,” *IEEE*
 485 *Transactions on Communications*, vol. 22, no. 5, pp. 637–648, 1974.
- 486 [39] G.-A. Fuglstad, F. Lindgren, D. Simpson, and H. Rue, “Exploring a new class of non-
 487 stationary spatial gaussian random fields with varying local anisotropy,” *Statistica Sinica*,
 488 pp. 115–133, 2015.

- 489 [40] C. S. Kulkarni and P. F. Lermusiaux, “Three-dimensional time-optimal path planning in
490 the ocean,” *Ocean Modelling*, vol. 152, p. 101644, 2020.
- 491 [41] M. J. Kuhlman, D. Jones, D. A. Sofge, G. A. Hollinger, and S. K. Gupta, “Collaborating
492 underwater vehicles conducting large-scale geospatial tasks,” *IEEE Journal of Oceanic
493 Engineering*, vol. 46, no. 3, pp. 785–807, 2021.